DNA-Silica Nanolattices as Mechanical Metamaterials

John Kulikowski^{1#}, Shuang Wang^{2#}, Zachary Aitken³, Jack Grimm^{4,5}, Baisen Gao⁶, Melody M. Wang⁷, David Doan¹, Andrew C. Lee⁷, Luyao Shen², Wei Huang⁶, Arun Devaraj⁵, Yong-Wei Zhang³, Yonggang Ke², X. Wendy Gu^{1*}

Affiliations

¹Department of Mechanical Engineering, Stanford University, Stanford, CA, 94305, USA

² Wallace H. Coulter Department of Biomedical Engineering, Georgia Institute of Technology and Emory University, Atlanta, GA, 30322, USA

³Institute of High Performance Computing (IHPC), Agency for Science, Technology and Research (A*STAR), 1 Fusionopolis Way, #16-16 Connexis, Singapore 138632, Republic of Singapore

⁴Materials Science and Engineering and Engineering, University of Washington, Seattle, WA 98195, USA

⁵Physical and Computational Sciences Directorate, Pacific Northwest National Laboratory, Richland, WA 99354, USA

⁶School of Aeronautics, Northwestern Polytechnical University, Xi' an, 710072, China

⁷Department of Materials Science and Engineering, Stanford University, Stanford, CA, 94305, USA

*These authors contributed equally to this work

*Corresponding author: X. Wendy Gu: <u>xwgu@stanford.edu</u>

*Lead contact: X. Wendy Gu: xwgu@stanford.edu

Summary

- 1 Mechanical metamaterials consist of periodic structures with enhanced material properties. The
- 2 best additive manufacturing techniques have resolutions of 100s of nanometers which cannot
- 3 fully realize material size effects. Further, they cannot easily combine disparate materials (e.g.,
- 4 soft, biological polymers with hard ceramics). Here, DNA origami is used to construct
- 5 octahedral-based isotropic and anisotropic nanolattices which are coated with silica. These DNA
- 6 nanolattices have features two orders of magnitude smaller than additively manufactured lattices
- 7 and obtain material properties comparable to the best nanolattices, due to material size effects.
- 8 Atom probe tomography confirms the nanoscale distribution of DNA and silica in the octahedral
- 9 lattice. Finite element modeling (FEM) reveals two dominate failure modes: buckling at lower
- 10 coating thicknesses and tensile fracture at higher thicknesses. Molecular dynamics (MD)
- simulations reveal that the DNA suppresses global buckling modes in favor of surface buckling
- which delays failure and contributes to increased strength at large strains.

Keywords: Self-assembly; Nanomaterials; Mechanical; Strength; Energy absorption; DNA origami; Composites; Architected Materials; Molecular dynamics; Finite element; Atom probe tomography

Introduction

13 Architected metamaterials with nano and microscale features have record strength, energy absorption¹, and stiffness per weight, as well as properties such as high recoverability under large 14 strains^{2,3} and negative Poisson's ratio⁴. These extraordinary properties arise from the combination 15 of an optimized 3D architecture, material properties and sample dimensions^{5,6}. Strut-based 16 lattices have properties such as high strength per weight, 5,7 but tend to buckle and undergo 17 localized deformation. Plate-based structures⁸, triply periodic minimal surfaces⁹, and tensegrity 18 lattices¹⁰ overcome these shortcomings by minimizing stress concentrations and effectively 19 transferring load. Enhancements in strength, stiffness and fracture toughness have been observed 20 in nanoscale metals, ceramics and polymers¹¹⁻¹⁶. Thus, reducing the feature size of architected 21 metamaterials to the nanoscale can improve mechanical performance without adding weight⁵. 22

Scalable fabrication of nano-architected metamaterials remains challenging. Stereolithography 23 and two-photon lithography are high-resolution additive manufacturing techniques for printing 24 polymeric lattices with features down to ~20 μm, and ~300 nm, respectively ^{17,18}. Resins have 25 been developed to directly print nanocomposite¹, semiconductor¹⁹ and piezoelectric²⁰ lattices. 26 Glassy carbon and metallic lattices can be achieved through the pyrolysis²¹ or chemical reduction 27 of two-photon lithographed lattices²². Metal, ceramic and hybrid nanolattices have also been 28 fabricated by printing a polymeric scaffold and then depositing an inorganic coating via 29 sputtering^{2,3}, electroless plating²³, or atomic layer deposition²⁴. This produces core-shell^{2,3} or 30 hollow lattices^{23,24} with shell thicknesses down to tens of nanometers, and unit cells of a few 31 microns in size. These lattices exhibit size effects in strength but are prone to buckling due to the 32 high aspect ratio of the thin shell coatings. 33

These additive manufacturing techniques print structures point-by-point or layer by layer, with 34 volumetric throughputs of $0.02 \text{ mm}^3/\text{h} - 6000 \text{ mm}^3/\text{h}$, such that a $3 \times 3 \times 3$ lattice takes minutes to 35 hours to print. There is a tradeoff between resolution and speed²⁵, which means that the 36 ultrasmall feature sizes in mechanical nano-lattices are slow to print. Colloidal self-assembly, 37 dealloying of metals and spinodal decomposition are alternative methods for the rapid fabrication 38 of centimeter scale samples, in which nano and microscale features are formed in parallel. These 39 methods are limited to randomly porous or simple periodic structures^{26,27}. For instance, self-40 assembled polymer spheres can be used as templates for silica, face-centered cubic inverse opal 41 structures²⁸, but alternative geometries with superior mechanical properties cannot be achieved. 42

Recent advances in DNA self-assembly allow for the fabrication of arbitrary 3D shapes with resolution of a few nanometers^{29–31}. Programmable control of geometry is achieved through DNA nucleotide pairing. Complex 3D lattice structures with features on the order of 6 nm can be fabricated, which is at least 2 orders of magnitude smaller than typical additive manufacturing techniques. Small DNA objects can be further assembled into larger structures. Towards this end, researchers have successfully assembled DNA origami^{30,32} monomers into microscale 3D

49 superlattices with tetrahedron³³, tensegrity triangle³⁴, cube, and octahedron geometries³⁵.

50 Different superlattice geometries can be achieved through control of the building blocks^{34–36},

51 connection valence strength³⁷, and the surrounding environment³⁸.

However, DNA is a soft material, which limits the load bearing ability of DNA lattices, despite 52 their programmable, intricate nanoscale structures. Post-assembly modifications have been 53 developed to enhance the rigidity of DNA structures. DNA structures have been used as 54 templates to grow or incorporate inorganic materials, including silica^{29,36}, silicon³⁹, and metals⁴⁰. 55 Individual DNA tetrahedra that are coated with silica³⁶ or stained with uranyl acetate⁴¹ have been 56 57 shown to have much higher elastic modulus than the bare DNA tetrahedra. Silica coated, face centered cubic DNA-nanoparticle lattices have previously been compressed under high 58 hydrostatic pressure in a diamond anvil cell⁴². Li et al. assembled DNA-metal nanoparticle 59 nanolattices with high strength and elastic modulus, but high densities compared to other 60 lightweight nanolattices⁴³. Michelson et al. used DNA origami to fabricate octahedral DNA 61 templates that were coated with silica, heat treated to solidify the SiO₂ and remove the DNA, and 62 then tested in compression for a single silica shell thickness (relative density)⁴⁴. Here, we use 63 similar methods to fabricate DNA core-silica shell nanolattices with isotropic and anisotropic 64 unit cells, and a variety of silica shell thicknesses, in order to investigate the influence of 3D 65 architecture and nanoscale material interactions on mechanical behavior. In our work, we show 66 67 that DNA-silica lattices have specific strength and energy absorption on par with the best 3D printed mechanical metamaterials and determine plasticity and failure mechanisms. Experiments 68 and computational simulations show that the nanoscale silica coating thickness is found to have a 69 dramatic effect on mechanical properties due to material size effects and leads to highly resilient 70 lattices when combined with DNA. The DNA core is found to improve the mechanical 71 performance at low silica coating thicknesses. 72

Results and Discussion

89

DNA origami is used to create the lattice structure. Using a previously published design²⁹, a 73 symmetric octahedral DNA origami is used as a building block, and corresponding DNA staple 74 sequences were generated with caDNAno⁴⁵. DNA origami monomers were prepared by mixing 75 the staples strands with a M13mp18 viral scaffold DNA strand in aqueous solution, which was 76 then subjected to a thermal annealing process³⁰. The octahedral monomer contains 12 structurally 77 identical struts. Each strut is composed of a six-helix bundle with a dimension of 28.6 nm in 78 length and 6 nm in diameter (Figure S1A). To form a 3D lattice, two octahedron monomers were 79 prepared separately and connected vertex-to-vertex via hybridization between complementary 80 DNA linkers (Figure S1B). Each octahedron vertex consists of four single-stranded linkers. 81 Every linker contains three domains: a 42-nucleiotide (nt) staple domain that binds stably to the 82 scaffold DNA, a 22-nt non-binding polythymine (polyT) in the middle to provide sufficient 83 flexibility, and an 8-nt sticky end (a sequence that is complementary to its counterpart on the 84 other DNA octahedron). The length of polyT domains and sticky ends were carefully screened in 85 a previous study for optimal lattice growth³⁰. 86

After assembly of the 3D DNA lattices, the structures were reinforced by silicification with a modified Stöber reaction⁴⁶. Briefly, the negative-charged surface of the DNA lattice adsorbs the

positive-charged precursor molecule N-trimethoxysilylpropyl-N,N,N-trimethylammonium

90 chloride (TMAPS). Then, tetraethyl orthosilicate (TEOS) is added and reacts with the TMAPS to form a silica coating over the DNA lattice via hydrolysis and co-condensation (Figure S1C; more 91 details can be found in Supplementary Information). This forms nanometer-thick coatings, which 92 retain the shape of the DNA lattice, and allows direct characterization with TEM and SEM 93 (Figures S2-S6). The final product of DNA-silica lattices are multiscale structures (Figure 1)²⁹. 94 Each unit cell (a DNA octahedron and its surrounding space) is approximately 50 nm×50 nm×50 95 nm in size. The lattice structures grow into uniform cubes consisting of thousands of unit cells 96

that are on the order of 10 µm in size. This lattice differs subtly from the octahedral lattice⁴⁷ due 97 to the short DNA linkers that connect the vertices of octahedral unit cells. 98

99 The thickness of the silica coating can be modulated by tuning reactant concentrations and reaction times. Samples were fabricated with coating thicknesses from ~1.65 nm to 5.1 nm 100 (Figure 2). These thicknesses were estimated from high resolution SEM images (Figure S12). A 101 near space filling coating was fabricated as well. These samples correspond to relative densities 102 from 9% to 91% when only considering the silica. The DNA itself takes up an additional ~9% of 103 the volume. These relative densities are higher than other nano-lattices with ~20-50 nm 104 coatings^{23,48}, because the DNA lattice unit cell is ~50 nm in size, while nano-lattices made 105 through lithographic methods have unit cells of ~10 µm in size^{23,24}. Approximately 1 out of 30 106 lattice struts is a vacancy defect that occurs randomly during the self-assembly process (details in 107 Supplementary Information). 108

Atom probe tomography (APT) was performed on the space filling DNA-silica lattice to provide 109 nanoscale elemental mapping. APT succeeded in identifying molecules containing C, N, and P, 110 which originate from DNA. Additionally, a small amount of Mg was found adsorbed to the 111 DNA. This is expected because Mg is used in the buffer solution used in self-assembly. Figure 112 2F shows the concentration of each ionic species as a function of the distance from C. This 113 shows that the concentrations of the organic species (N, Mg, CN, PO) are elevated in the 114 presence of C whereas inorganic species (Si, SiO, SiO₂) are depleted. The detected C is assumed 115 to be in the DNA backbone. A heatmap of the organic-to-inorganic ratio from a 6 nm-thick slice 116 through the lattice shows that organic-rich volumes appear at the expected distances for the 117 118 octahedral lattice struts (Figure 2G). This analysis suggests that the silica coating is in fact evenly and conformally coated across the DNA structure without damaging or distorting the 119 120 underlining lattice structure. Further, it suggests that the lattice with the space filling coating is a solid or nearly solid structure because inorganic markers are found throughout the DNA depleted 121 122 regions.

Anisotropic octahedral DNA lattices were also assembled (details in Supplementary 123 Information). As shown in Figure 3A-C, the standard octahedral lattice has a unit cell with an 124 125 aspect ratio of 1:1:1, while the elongated lattice has a unit cell that is a rectangular prism with an expected aspect ratio of ~1.4:1:1 (this ratio corresponds to the x:y:z coordinates, where y is the 126 out of plane direction in figure 3A-C). The flattened lattice has a unit cell that is a rectangular 127 prism with an expected aspect ratio of ~1.7:1.7:1. From the top view, the standard lattice unit cell 128 and the flattened lattice unit cell appear isotropic, while the elongated lattice appears anisotropic. 129 From the side view, both the elongated and flattened lattice appear anisotropic. The strut length 130

- in the standard lattice is 28.6 nm. In the elongated lattice, the strut lengths are increased to 35.7
- nm along two axes, and remains 28.6 nm along one axis. In the flat lattice, the strut length is
- increased to 35.7 nm along one axis, and remains 28.6 nm along two axes. The elongated lattice
- has a silica coating of 2.29 nm while the flat lattice has a silica coating of 1.33 nm. SEM imaging
- shows that the actual aspect ratios are 1.5:1.2:1 and 2.4:2.3:1 for the elongated and flattened
- lattice, respectively. These results demonstrate the range of DNA crystals that can be achieved
- by designing the corresponding building blocks.
- In-situ SEM mechanical testing is used to compress the lattices with 1.75, 3.1, and 5.1 nm silica
- thickness with a diamond flat punch tip. Michelson et al. showed that DNA-templated silica
- 140 lattices with larger sizes tend to have a higher concentration of defects, leading to worse
- mechanical performance⁴⁴. For this reason, cubes of 2-4 µm in side length were chosen for
- 142 mechanically testing in our study. The mechanical properties of the DNA-silica samples are
- plotted against cube size in Supplementary Figure S16.
- 144 Compression of lattices with a 1.75 nm coating thickness resulted in two types of stress-strain
- curves. The first curve, which is shown in Figure 3D in blue, has an elastic modulus of 232 MPa
- up to $\sim 60\%$ strain, at which point the modulus increases due to densification. The stress-strain
- 147 curve has a smooth shape without sudden displacement events. This stress-strain curve
- 148 corresponds to the lattice in Figure 3E, which formed vertical cracks during compression. The
- second curve (green) has an elastic modulus of 812 MPa, and initial fracture stress of 200 MPa.
- 150 The initial fracture strength is defined as the onset of the first zero or negative stiffness regime.
- 151 This stress-strain curve corresponds to the formation of diagonal (~45°) cracks (Figure 3F),
- which can be observed on in-situ deformation videos (see supplementary videos, S1-S5).
- 153 The 3.1 nm and 5.1 nm lattices tend to form vertical cracks while the space filling lattice tends to
- form horizontal cracks (Figure S10). Smooth stress-strain curves were observed for the 3.1 nm
- lattice. The 5.1 nm and space filling lattices have stress-strain curves with sudden drops in stress
- at high strains. The 3.1 nm and 5.1 nm lattices have failure stresses of 1.6 ± 0.8 GPa and $1.0 \pm$
- 157 0.2 GPa, respectively, and elastic moduli of 3.2 ± 2.2 GPa and 4.4 ± 1.0 GPa, respectively.
- Lattices with 1.65 nm and 2.1 nm silica coating were compressed in a benchtop nanoindenter
- 159 (see Supplementary Figure S15). These samples show similar mechanical performance to the
- 160 1.75 nm sample (Supplementary Table 1 lists the measured yield strength of each sample).
- Without the video capabilities of in-situ testing, an exact fracture point cannot be determined.
- Instead, a 1% offset yield⁴⁴ stress is used to characterize the strength of the structures.
- Anisotropic lattices were compressed using a benchtop nanoindenter in the geometry shown in
- Figure 3B-C. The elongated and flat octahedral lattices display similar stress-strain behavior
- before yield, but distinct post-yield behavior. Elongated octahedral structures have an elastic
- modulus of 810 ± 400 MPa and a 1% yield stress of 95 ± 67 MPa while the flattened octahedral
- structures have an elastic modulus of 630 ± 400 MPa and 1% yield stress of 126 ± 52 MPa. The
- 168 elongated octrahedral structure exhibits dips in the stress-strain plot consistent with layer-by-
- layer failure or cracking, which is corroborated by post-compression imaging (Figure 3H). The
- 170 flattened octahedral structure instead has an elastic region followed by a subtle yield point and
- 171 no evidence of fracture, which is consistent with post compression imaging (Figure 3I). This may
- be due to the pancake-like aspect ratio of the flattened samples.

173 The 1% offset yield stress of the DNA-silica lattices is compared to other nano-lattices in Figure 174 4A. The DNA-silica lattices are also highly deformable, reaching strains of 30% or more without significant fracture events. This leads to extremely high energy absorption before fracture of ~50 175 176 MJ/m³, 340 MJ/m³, 180 MJ/m³, and 270 MJ/m³ for the 1.75 nm, 3.1 nm, 5.1 nm, and space filling standard lattices, respectively (Figure 4B). Energy absorption is an important property of 177 impact resistant materials. The specific strength and energy absorption of the DNA-silica lattices 178 are similar to glassy carbon plate-lattices⁸ and spinodal structures⁴⁹, and are well above the 179 180 performance of conventional engineering materials and other strut-based nanolattices. The elastic modulus of the DNA-silica lattices is in the range of 0.5-5 GPa, which is comparable to other 181 ceramic nano-lattices (Figure 4C). The observed compressive strength values are similar to that 182 of bulk silica (1-1.6 GPa). The elastic moduli of the tested sample, however, are significantly 183 lower than that of bulk silica (~72 GPa). This results in a significantly higher strain at failure and 184 energy absorption when compared to bulk silica. The energy absorption of bulk silica is 185 estimated to be \sim 18 MJ/m³ from a linear elastic strain energy density function. 186

Surprisingly, the elastic modulus and strength of the lattices do not monotonically increase with increasing density. Instead, the elastic modulus and strength of the 3.1 nm and 5.1 nm lattices are higher than lattices with lower or higher coating thickness. To understand this, the 3D architecture of the isotropic DNA-silica lattice is considered. Traditionally, a 3D lattice can be considered stretching dominated if the relative density is below ~10% and the number of nodes and struts in a unit cell satisfies the following⁷:

$$s-3n+6\geq 0\tag{1}$$

where s is the number of struts and n is the number of nodes. The DNA-silica lattice unit cell has 15 struts and 6 nodes so it is stretching dominated, which means that the dominant deformation of each strut will be either simple tension or compression along its long axis. A simple pin-joint analysis can be used to predict elastic modulus and strength. We assume a homogeneous and isotropic material, cylindrical struts, and frictionless pins at the nodes. This analysis (see Supplementary equations S.1-S.17) results in the following first order scaling laws:

$$E_{lattice} = 0.12 E_{bulk} \overline{\rho} \tag{2}$$

$$\sigma_{lattice} = 0.26 \,\sigma_{bulk} \,\overline{\rho} \tag{3}$$

where $E_{lattice}$ and $\sigma_{lattice}$ are the elastic modulus and yield strength of the lattice, E_{bulk} and σ_{bulk} are the elastic modulus and yield strength of the bulk material, and $\overline{\rho}$ is the relative density of the lattice. The linear scaling of elastic modulus and strength with relative density is the same as other stretching dominated lattices⁵.

Equation 2 and 3 are applicable to relative densities up to ~10%^{5,54}. For relative densities up to ~30%, structures can still be considered as open cell foams, but will have scaling coefficients larger than one due to the influence of bending. For higher relative density lattices, the 1st order approximations no longer hold; instead, the nonlinear Hashin-Shtrikman bound and Suquet bound can be used to predict the maximum elastic modulus and failure strength for a porous

material⁵⁵. The Hashin-Shtrikman upper bound on modulus (E_{HS}) and Suquet bound for strength (σ_{Su}) can be calculated as the following^{5,8}:

$$E_{HS} = \frac{2\overline{\rho}(5\nu - 7)}{13\overline{\rho} + 12\nu - 2\overline{\rho}\nu - 15\overline{\rho}\nu^2 + 15\nu^2 - 27}E_{bulk}$$

$$\tag{4}$$

$$\sigma_{Su} = \frac{2\,\overline{\rho}}{\sqrt{4 + \frac{11}{3}(1 - \overline{\rho})}} \sigma_{bulk} \tag{5}$$

where *v* is the Poisson's ratio of the material. For the DNA-silica lattices, we observe strengths above the Suquet prediction (Figure 4) for bulk material. Typical lattice materials do not approach either bound for strength or elastic modulus, and if they do, they are meticulously designed structures^{8,56}. However, the experimental strength values for some of the 1.75 nm and 3.1 nm silica coatings samples lay above the Suquet bound. This indicates that size effects must occur within the nanoscale silica coating to enhance the material properties compared to the bulk material.

At ultrasmall sizes, mechanical strength can be significantly improved compared to their macroscale counterparts⁵. For brittle materials, the effect of the nanoscale sample size on strength can be obtained using Griffith's law⁵. Griffith's law states the relationship between fracture stress ($\sigma_f \dot{c}$ and critical crack size (a_c) to be:

$$\sigma_f = Y \frac{K_{IC}}{\sqrt{\pi a_c}} \tag{6}$$

where Y is a geometric parameter and K_{IC} is the fracture toughness. a_c is taken to be equal to half 221 the thickness of the silica coating. Due to the inverse relationship between σ_f and a_c , the effect 222 becomes more pronounced at the nanometer scale. The theoretical strength for silica is \sim 22 GPa 223 when approximated as $\frac{E_{57}}{\pi}$. Based on equation 4, this strength is reached for a silica coating 224 thickness of ~1 nm (the thinnest silica coating is ~1.65 nm). The gradient theoretical bound 225 shown in Figure 4A uses the bulk properties of silica for the lower bound and replaces σ_{bulk} in 226 equation 5 with the theoretical strength of silica for the upper bound. We ignore the properties of 227 228 DNA in this analysis because silica has 2-3 orders of magnitude higher modulus and strength than DNA. For instance, DNA has an elastic modulus of ~300 MPa - 1 GPa^{58,59}, which is 229 considerably lower than that of bulk silica (~72 GPa). Yet, the addition of DNA may impact the 230 failure mode and therefore the failure stress. The DNA should not affect the elastic regime, but 231 may affect the mechanical behavior of the lattice at large strains⁶⁰. 232

Pin-joint analysis indicates that uniaxial compression of the lattice leads to compression in struts that are aligned with the loading direction (vertical struts), and tension in struts that are perpendicular to the loading direction (horizontal struts) (see equations S.2 and S.4), which is corroborated by finite element modeling (FEM) (see Supplemental Figures S24-26). Buckling is an expected failure mode of slender rods or hollow struts in compression. The shell buckling criterion for a hollow strut with a thin shell is:

$$\sigma_{buckle} = \frac{E_{bulk}}{\sqrt{3(1-v^2)}} \left(\frac{t}{R}\right) \tag{7}$$

where t and R are the thickness of the shell and radius of the strut, respectively. This suggests a critical buckling load of ~19 GPa for a hollow strut with a silica coating thickness of 1.65 nm. If it is assumed that tensile (horizontal) struts approach the theoretical strength for silica, then compressive (vertical) struts should buckle before the tensile struts fail. For larger coatings, equation 7 predicts values significantly higher than the theoretical strength of silica, which indicates that buckling is unlikely in these samples.

FEM simulations are implemented to understand the deformation and failure modes of the lattice structure. Simulations are performed on a hollow silica shell lattice consisting of 3x3x3 unit cells with different silica shell thickness. Simulations are also performed on a DNA lattice and a DNA-silica lattice to small strains (see Supplemental S28). Once the hollow silica shell thickness is large enough to prevent buckling, the FEM stress-strain response agrees with experiment. This is the case for the stress-strain curves shown in Figure 5A. The thinner coating (~1.4 nm) shown in Figure 5B fails via a collapsing of the structure at the vertically aligned joints while the thicker coating (~4.4 nm) shown in Figure 5C fails via tensile fracture at the horizontally aligned joints. These results indicate that the high stiffness and strength observed in the experimental thin silica shells is likely due to the presence of the DNA core. This is further explored in molecular dynamics simulations.

Molecular dynamics (MD) simulations are used to investigate the role of the DNA on mechanical behavior in the post-buckling regime. Individual struts, rather than an entire unit cell, are studied. The compressive stress-strain curves from MD simulations are shown in Figure 5D. Two samples are simulated: a hollow silica strut, and a DNA core-silica shell strut. The shell thickness is 1 nm for both samples, and the strut diameter is 6 nm, which corresponds to the experimental lattices. To explore the effect of the DNA core, each strut was subjected to a set of boundary conditions on the inner surface. The first set of boundary conditions simulated the presence of a stiff DNA core by specifying a reflective wall at the inner diameter. This prevents inward radial deformation of the silica wall and off-axis bending of the silica wall. The second set of boundary conditions removed these restrictions and allowed for full displacement of the silica wall, to simulate a hollow silica strut. For both samples, stress-strain data indicate an initial linear elastic loading segment with an average slope of 76 GPa. Stress begins to diverge from this linear segment at ~4% strain. For the hollow silica strut, stress reaches a maximum of 3.2 GPa after which the stress decreases. For the DNA core-silica shell strut, stress continues to increase for the remainder of loading, after diverging from the initial linear segment.

The final atomic configurations are shown in Figure 5E and 5F for the two samples. Without the internal boundary condition, the hollow silica strut undergoes local buckling and forms an off-axis kink. With a rigid boundary condition, the DNA-silica strut undergoes local buckling, but wrinkles along the loading axis. The presence of the DNA interior modifies the buckling behavior of the compressive struts, resulting in a wrinkling type buckling mode as opposed to a kinking mode and prevents the appearance of a negative stiffness regime in the stress-strain plot.

The pre-buckling behavior is largely unaffected by the presence of DNA. The DNA increases the sustained stress at high strains and suppresses the negative stiffness regimes in the compressive struts. Globally, this results in a smoother stress-strain curve without sudden, progressive failure events like those observed in other ceramic nano-lattices⁴⁹. It is therefore likely that the peaks observed in the experimental stress-strain plots correspond to local tensile failures leading to global crack formation. Figure S31B shows the compressive stress-strain data for struts with 2 nm silica shell thickness, which qualitatively agree with the results on 1 nm shell thickness shown in Figure 5.

MD simulations of hollow silica and DNA-silica struts in tension show linear elastic behavior, followed by sudden failure at high stresses (>20 GPa) (see Figure S31D-E). The two separate regimes observed in the 1.75 nm samples may be explained by two separate buckling modes causing a difference in the modulus and fracture behavior at higher strains or by earlier local tensile failures due to preexisting flaws in some samples. These MD results complement the FEM results and show that the silica shell only is not sufficient to model the behavior of the thinner shell thicknesses in the post buckling regime. Indeed, the change in buckling mode due to the presence of the DNA core leading to sustained load bearing likely accounts for the difference between the experimental and FEM simulated structures with low shell thicknesses.

Conclusion

This work demonstrates that DNA self-assembly can produce high performance mechanical metamaterials. We find that octahedral DNA lattices that are coated with silica have specific strength and energy absorption as high as 2.5 GPa cm³/g and 540 J/g, respectively, which is on par with the best lithographed nanolattices. The DNA-silica lattices are made of ultrasmall—and therefore ultra-strong— materials. The ~50 nm sized unit cell is 2-3 orders of magnitude lower than what is achievable using lithography. This, combined with the nanoscale silica coating thickness results in strong material size effects that lead to strength above the Suquet upper bound for bulk silica. The DNA interior likely suppresses global buckling modes in favor of surface modes which suggests that the global failure events observed experimentally correspond to an accumulation of tensile failures.

3D architectures such as the octet⁷, tensegrity¹⁰, plate lattices⁵⁶, and triply periodic minimal surfaces⁹ have better mechanical performance compared to the simple octahedron unit cell in this study. Despite this, the DNA-silica lattices outperform nanolattices with these optimized architectures. This indicates that further improvements can be achieved by expanding the geometries of DNA lattices in the future. Additional DNA staple strands can be added to strengthen stress concentrations, such as the nodes between lattice struts. Different materials such as metals could be deposited on the DNA lattices⁶¹, to create highly recoverable structures that still benefit from nanoscale size effects⁵. In this way, additional properties such as high electrical conductivity, thermal conductivity, and optical reflectivity could also be introduced. The use of DNA self-assembly demonstrates a pathway for the scalability challenges of architected metamaterials, in which bottom-up self-assembly methods are used for massively parallel nanofabrication⁶².

Resource Availability

Lead Contact: Further information and requests for resources should be directed to and will be fulfilled by the lead contact, Wendy Gu (xwgu@stanford.edu)

Materials Availability: This study did not generate new unique reagents. DNA-silica lattices presented can be reproduced following the procedure described in the experimental procedures below.

Data and Code Availability: Data needed to reproduce the results can be found in the Dryad repository: https://doi.org/10.5061/dryad.g4f4qrfxz

Experimental Procedures

- 316 Design and synthesis of octahedron unit cell: Octahedron framework is designed by caDNAno
- software (http://cadnano.org/) and synthesized by mixing P7249 scaffold strand (extracted from
- 318 M13 bacteriophage) and unpurified DNA staple strands (see Supplementary tables) in 1×TAE
- buffer (40 mM Tris, 1 mM EDTA, pH 8.3) containing 12.5 mM MgCl₂ and thermal annealing
- ramps from $90\Box$ to $20\Box$ for 24 h in a PCR thermos cycler (S1000 Thermal Cycler, Bio-Rad).
- Each edge of the frame is composed of a six-helix bundle with 28.6 nm (84 base pairs) in length
- and 6 nm in diameter. Two single strands (sticky ends) stretch out from two ends of one 6HB
- 323 respectively, and four sticky ends extend from one vertex.
- 324 Design and assembly of DNA lattice: The DNA lattice was assembled by combining two kinds
- 325 of octahedron frames with complementary sticky ends in an equal molar concentration and
- carrying out a slow annealing ramp from $50\Box$ to $20\Box$ in 150 h. The base pairing interaction from
- 327 vertex-to-vertex hybridization and slow annealing lead to formation of crystal habits with
- 328 minimal surface energy.
- SiO_2 growth protocols: The silicification is based on the modified Stöber reaction by adding two
- 330 silica precursors TMAPS and TEOS in sequence. Briefly, the quaternary ammonium group in
- 331 TMAPS with positive charge binds with the anionic DNA phosphate backbone by electrostatic
- 332 attraction. The siloxane group on TMAPS and TEOS go through hydrolysis and co-
- condensation, forming connective siloxane bridges (Si-O-Si). Considering the competitive effect
- between TMAPS and magnesium ions, we wash the sample with 1×TAE buffer containing 7
- 335 mM MgCl₂ several times to lower the magnesium concentration. Then, TMAPS is added into the
- DNA lattice sample at room temperature and shaken on a vortex mixer at a rate of 400 rpm for
- 337 20 min. The absorption of TMAPS on the DNA double-strand backbone determines the
- condensation sites and distribution of the silica coating. Later, TEOS is added into the solution
- and shaken for another 30 min at same rate. After completing the addition of the two silica
- and shaken for another 50 mm at same rate. Their completing the addition of the two since
- 340 precursors, the mixture is kept static for 12 h at room temperature. A cloudy precipitate will
- 341 appear at the bottom of tube, which indicates the completion of the DNA lattice silicification and
- 342 formation of silica clusters in solution. After washing with deionized water several times, some
- 343 isolated silica clusters are removed.
- 344 SiO₂ thickness control: The silica thickness is related to several parameters including the
- concentration of the DNA lattice (all the nucleotides) and the two silanes (TMAPS and TEOS).

We mix the DNA lattice sample and the two silanes (nucleotide: TMAPS: TEOS) in different molar ratio. According to the nucleotide quantities of DNA lattice sample in the solution, we add different amounts of silanes. Here, we add TMAPS and TEOS according to the reported ratio of 1:10:20, which forms ~1.75 nm silica coating. As mentioned earlier, TMAPS absorption on the

350 crystal produces the nucleation sites for silicification, and is vitally important for the uniform-

351 distribution of silica on the microstructure. We modified this silica precursors ratio by changing

352 the TEOS amount to modulate the thickness of silica on the DNA lattice.

353 Liftout and sharpening: For atom probe tomography (APT), it is necessary to shape a sample into a needle with a tip diameter <~100 nm. This was achieved using a dual-beam plasma focused ion 354 beam scanning electron microscope (FIB-SEM, Hydra, Thermo Fisher) equipped with a 355 nanomanipulator (EZLift, Thermo Fisher). A 0.5 µm-thick protective capping of Pt was 356 deposited on the (100) surface of a space filling DNA nanolattice using a 30 kV 0.1 nA Xe ion 357 beam. While keeping the (100) surface normal to the ion beam, rectangular patterns were then 358 used with the 30 kV 0.1 nA ion beam to remove the excess material on either side of the Pt cap. 359 Cleaning cross sections were then used with 30 kV 0.1 nA ion beam to thin the lamella and 360 polish the sides. The stage was tilted back to 0° (i.e. (100) surface normal to electron beam), then 361 a small deposition of Pt was deposited with a 30 kV 30 pA ion beam to attach the lamella to the 362 nanomanipulator. A cleaning cross section pattern was then used to make an undercut with 30 363 kV 30 pA ion beam, separating the lamella from the substrate and causing the bottom face of the 364 lamella to be at a 52° angle (the same angle between the ion beam and electron beam). Silicon 365 366 microposts (m22 array, Cameca) were similarly milled to allow for a flush contact between the micropost and sample lamella, then Pt depositions used to secure the sample (Figure S8). 367

Annular ion beam milling patterns at 30 kV 0.1—0.03 nA with progressively decreasing outer and inner diameters (4—3.5 µm and 1.2—0.3 µm, respectively) were used to shape the liftout into a needle, then finally sharpened to a final tip diameter <100 nm with a 5 kV 10 pA ion beam "shower" with no pattern (Figure S8).

Atom Probe Tomography: APT experiments were conducted on a local electrode atom probe 372 6000 (LEAP 6000 XR, Cameca). The new simultaneous voltage pulse mode—a capability of the 373 LEAP 6000 not seen in previous generations of atom probe wherein the ~1 ns pulse of the 374 λ =257.5 nm wavelength laser used to stimulate ion evaporation is timed to overlap with a brief 375 376 increase in the applied voltage—was used for this experiment. This new approach is purported to decrease the noise floor in the collected mass-to-charge spectra by decreasing the standing 377 electric field between pulses, reducing the chance for unintended/mistimed evaporation events. A 378 5% voltage pulse fraction was used in conjunction with a 3.5-10 pJ laser pulse energy at a pulse 379 frequency of 100 kHz. A 1% target detection rate was maintained using the "rapid" voltage 380 control algorithm. The specimen base temperature was maintained at 40 K. 381

Data processing, three-dimensional reconstructions, and APT analysis were conducted in the integrated visualization and analysis software module of APSuite (version 6.3, Cameca). The mass-to-charge spectrum contained many (>100) peaks. For this study, only those peaks with signal exceeding double the surrounding background when using a bin size of 0.005 Da were ranged and identified (Figure S9). To help ensure the accuracy of the mass-to-charge spectra,

387 only select prominent peaks with a clear identity were used for the peak calibration stage of

processing and are listed in the Supplemental Information. The tip profile was measured from a 388

high-resolution SEM micrograph (Figure S8) of the final sample shape to guide the radius 389

evolution during reconstruction, in addition to setting Si as the primary element with an 390

- evaporation field of 33 V/nm. 391
- 392 In the reconstruction analysis, custom regions of interest can be imported as .STL files. The
- DNA origami octahedra unit cell was reproduced in AutoDesk Inventor 2023 at 106 scale (i.e. 1 393
- mm = 1 nm) and exported as a .STL file. Upon importing as ROI objects into APSuite, the scale 394
- is automatically adjusted such that the struts are 28.6 nm long with a diameter of 6 nm. 395
- Maneuvering an assembly of these ROI octahedra proved useful in validating the distribution 396
- and periodicity of the organic phase in the reconstruction (Supplementary Figure S9). 397
- 398 Mechanical characterization: Silica coated DNA lattices were drop cast on silicon wafer pieces.
- 399 Mechanical characterization was performed using the NanoFlip nanoindenter (KLA Corporation)
- in a FEI Helios Nanolab 600i DualBeam SEM or with a iMicro nanoindenter (KLA Corporation) 400
- benchtop system. Lattices were compressed to ~50-70% strain at a displacement rate of 10 nm/s 401
- using a 20 µm diamond flat punch tip. Each silica thickness is tested for at least 3 samples. SEM 402
- images were taken using a FEI Helios Nanolab 600i DualBeam or Thermo Fisher Scientific 403
- Apreo S LoVac SEM. 404
- 405 FEM simulations: Models are created in Solidworks 2022 and meshed in Hypermesh 2022 with
- the described geometry for the DNA-silica lattice. The octahedral unit cell is 47 nm in size, with 406
- DNA struts of 6 nm in diameter, and 28.6 nm in length. Numerical simulations are performed in 407
- 408 Abaqus 2023 with dynamic explicit for quasi-static loading analysis (the rate of kinetic energy
- and internal energy is within 5%) and linear perturbation for buckling mode analysis. Figure 5 409
- uses mesh assignments as provided in Supplementary Figure S30. For structures which consider 410
- the DNA core (Supplementary Figures S25-29), the silica coatings and DNA cores are meshed 411
- by shell elements and solid elements, respectively. The perfect contact interfaces are adopted 412
- between the DNA core and the silica shell. Hence, the coatings and cores are tied to ensure a 413
- coincident deformation for the DNA-silica lattice. For loading conditions, one side of the lattice 414
- is placed under a fixed boundary condition and the opposite side is given a prescribed 415
- displacement. 416

421

- 417 MD simulations: We employ molecular dynamics (MD) simulations to understand the
- deformation response of the amorphous DNA-silica nanolattices. The simulated sample matches 418
- 419 the geometry of a single strut of the experimental lattice. The length of the strut is 29.5 nm, and
- the inner diameter of the strut is 6 nm. We consider samples with silica thicknesses of 1 nm and 420
- 2 nm, which leads to an outer diameter of 8 nm and 10 nm. To construct an amorphous
- 422 microstructure, we follow a melt and quench methodology. We specify a mold using reflective
- walls following the geometries described above and populate the volume with Si and O atoms in 423
- a stoichiometry of 1:2 and with a density that approximates the experimentally known density of
- 424 2.2 g/cm³ for amorphous silica⁶³. These atoms were brought to 6000 K to the liquid phase and 425
- held there for 200 ps. The samples were then guenched to 300 K at a rate of 2 K/ps. The resulting 426
- 427 geometry is shown in Figure S17. Before applying deformation, all samples were thermalized at

428 300 K for 20 ps. Because various struts throughout the lattice experience stress states of tension and compression, all sample geometries were subjected to tensile (Figure S31D-F) and 429 compressive loading by changing simulation box size at a strain rate of 10⁹ s⁻¹ up to a final 430 engineering strain of 20%. Interactions among Si and O pairs were modelled using a Tersoff 431 potential developed by Munetoh, et al.⁶⁴ All simulations were performed using the LAMMPS 432 molecular dynamics software⁶⁵ and all steps of the simulation process were time integrated using 433 the NVT ensemble with an integration timestep of 1 fs. OVITO⁶⁶ was used for common neighbor 434 analysis (CNA), calculation of local atomic strain, and visualization of atomic configurations. 435 Stress and strain are calculated with reference to the initial sample geometry and only 436 considering the solid silica wall material. 437

Acknowledgements

438 This work was financially supported by the National Science Foundation (CMMI-2052251, CCF-2227399, and DMR-2002936/2002891). Part of this work was performed at the Stanford 439 Nano Shared Facilities (SNSF), supported by the National Science Foundation under award 440 ECCS-2026822. ACL acknowledges the Knight-Hennessey Scholarship. ACL and MMW are 441 supported by the National Science Foundation Graduate Research Fellowship under 442 Grant No. DGE-1656518. ZA and Y-WZ acknowledge the financial supports from the the AISG 443 Grand Challenge in AI for Materials Discovery (AISG2-GC-2023-010), the A*STAR SERC 444 CRF Award, and the use of computing resources at the A*STAR Computational Resource 445 Centre and the National Supercomputing Centre, Singapore. WH acknowledges the financial 446 supports from the National Natural Science Foundation of China (Grant No. 12172292). AD and 447 JG would like to acknowledge the funding from the NIH-NIDCR Grant number DE-015347 for 448 the atom probe tomography work conducted in PNNL. This research utilized PFIB and LEAP 449 6000 XR capabilities housed in the energy sciences center, procured using the PNNL 450 institutional investment. 451

452

Author Contributions

JK, MMW, DD, and ACL performed mechanical testing. SW designed and provided samples. JK and SW performed imaging. JK analyzed and curated data. ZA performed MD simulations. WH and BSG performed FEM simulations. JK, SW, ZA, and XWG wrote the manuscript. YK and XWG provided conceptualization and supervision. WH, YWZ, YK, and XWG provided expertise. JG and AD conducted the APT sample preparation and analysis and contributed to the manuscript drafting.

Declaration of Interests

The authors declare no competing financial interest.

References

- 1. Li, Q., Kulikowski, J., Doan, D., Tertuliano, O.A., Zeman, C.J., Wang, M.M., Schatz, G.C., and Gu, X.W. (2022). Mechanical nanolattices printed using nanocluster-based photoresists. Science *378*, 768–773. 10.1126/science.abo6997.
- 2. Zhang, X., Yao, J., Liu, B., Yan, J., Lu, L., Li, Y., Gao, H., and Li, X. (2018). Three-Dimensional High-Entropy Alloy-Polymer Composite Nanolattices That Overcome the Strength-Recoverability Trade-off. Nano Letters *18*. 10.1021/acs.nanolett.8b01241.
- 3. Feng, X., Surjadi, J.U., Fan, R., Li, X., Zhou, W., Zhao, S., and Lu, Y. (2021). Microalloyed medium-entropy alloy (MEA) composite nanolattices with ultrahigh toughness and cyclability. Materials Today *42*, 10–16. 10.1016/J.MATTOD.2020.10.003.
- 4. Wang, X.T., Li, X.W., and Ma, L. (2016). Interlocking assembled 3D auxetic cellular structures. Materials & Design *99*, 467–476. 10.1016/J.MATDES.2016.03.088.
- 5. Bauer, J., Meza, L.R., Schaedler, T.A., Schwaiger, R., Zheng, X., and Valdevit, L. (2017). Nanolattices: An Emerging Class of Mechanical Metamaterials. Advanced Materials *29*, 1701850. 10.1002/adma.201701850.
- 6. Surjadi, J.U., Gao, L., Du, H., Li, X., Xiong, X., Fang, N.X., and Lu, Y. (2019). Mechanical Metamaterials and Their Engineering Applications. Advanced Engineering Materials *21*, 1800864. 10.1002/adem.201800864.
- 7. Deshpande, V.S., Fleck, N.A., and Ashby, M.F. (2001). Effective properties of the octetruss lattice material. Journal of the Mechanics and Physics of Solids *49*, 1747–1769. 10.1016/S0022-5096(01)00010-2.
- 8. Crook, C., Bauer, J., Guell Izard, A., Santos de Oliveira, C., Martins de Souza e Silva, J., Berger, J.B., and Valdevit, L. (2020). Plate-nanolattices at the theoretical limit of stiffness and strength. Nature Communications 2020 11:1 *I1*, 1–11. 10.1038/s41467-020-15434-2.
- 9. Al-Ketan, O., Lee, D.-W., Rowshan, R., and Abu Al-Rub, R.K. (2020). Functionally graded and multi-morphology sheet TPMS lattices: Design, manufacturing, and mechanical properties. Journal of the Mechanical Behavior of Biomedical Materials *102*, 103520. 10.1016/j.jmbbm.2019.103520.
- 10. Bauer, J., Kraus, J.A., Crook, C., Rimoli, J.J., and Valdevit, L. (2021). Tensegrity Metamaterials: Toward Failure-Resistant Engineering Systems through Delocalized Deformation. Advanced Materials *33*. 10.1002/ADMA.202005647.
- 11. Miller, R.E., and Shenoy, V.B. (2000). Size-dependent elastic properties of nanosized structural elements. Nanotechnology *11*, 139. 10.1088/0957-4484/11/3/301.
- 12. Bažant, Z.P. (1999). Size effect on structural strength: a review. Archive of Applied Mechanics 69, 703–725. 10.1007/s004190050252.

- 13. Mathur, A., and Erlebacher, J. (2007). Size dependence of effective Young's modulus of nanoporous gold. Applied Physics Letters *90*, 061910. 10.1063/1.2436718.
- 14. Manoharan, M., Lee, H., Rajagopalan, R., Foley, H., and Haque, M. (2009). Elastic Properties of 4–6 nm-thick Glassy Carbon Thin Films. Nanoscale Research Letters 2009 5:1 5, 14–19. 10.1007/S11671-009-9435-2.
- 15. Wang, G., Najafi, F., Ho, K., Hamidinejad, M., Cui, T., Walker, G.C., Singh, C.V., and Filleter, T. (2022). Mechanical Size Effect of Freestanding Nanoconfined Polymer Films. Macromolecules *55*, 1248–1259. 10.1021/acs.macromol.1c02270.
- 16. Wang, S., Yang, Y., Zhou, L.M., and Mai, Y.-W. (2012). Size effect in microcompression of epoxy micropillars. J Mater Sci *47*, 6047–6055. 10.1007/s10853-012-6513-0.
- 17. Melchels, F.P.W., Feijen, J., and Grijpma, D.W. (2010). A review on stereolithography and its applications in biomedical engineering. Biomaterials *31*, 6121–6130. 10.1016/j.biomaterials.2010.04.050.
- 18. Harinarayana, V., and Shin, Y.C. (2021). Two-photon lithography for three-dimensional fabrication in micro/nanoscale regime: A comprehensive review. Optics & Laser Technology *142*, 107180. 10.1016/j.optlastec.2021.107180.
- 19. Liu, S.-F., Hou, Z.-W., Lin, L., Li, F., Zhao, Y., Li, X.-Z., Zhang, H., Fang, H.-H., Li, Z., and Sun, H.-B. (2022). 3D nanoprinting of semiconductor quantum dots by photoexcitation-induced chemical bonding. Science *377*, 1112–1116. 10.1126/science.abo5345.
- 20. Lu, H., Cui, H., Lu, G., Jiang, L., Hensleigh, R., Zeng, Y., Rayes, A., Panduranga, M.K., Acharya, M., Wang, Z., et al. (2023). 3D Printing and processing of miniaturized transducers with near-pristine piezoelectric ceramics for localized cavitation. Nat Commun *14*, 2418. 10.1038/s41467-023-37335-w.
- 21. Bauer, J., Schroer, A., Schwaiger, R., and Kraft, O. (2016). Approaching theoretical strength in glassy carbon nanolattices. Nature Materials 2016 15:4 *15*, 438–443. 10.1038/nmat4561.
- 22. Tanaka, T., Ishikawa, A., and Kawata, S. (2006). Two-photon-induced reduction of metal ions for fabricating three-dimensional electrically conductive metallic microstructure. Applied Physics Letters *88*, 081107. 10.1063/1.2177636.
- 23. Ye, J., Liu, L., Oakdale, J., Lefebvre, J., Bhowmick, S., Voisin, T., Roehling, J.D., Smith, W.L., Cerón, M.R., van Ham, J., et al. (2021). Ultra-low-density digitally architected carbon with a strutted tube-in-tube structure. Nature Materials 2021 20:11 *20*, 1498–1505. 10.1038/s41563-021-01125-w.
- 24. Meza, L.R., Das, S., and Greer, J.R. (2014). Strong, lightweight, and recoverable three-dimensional ceramic nanolattices. Science *345*, 1322–1326. 10.1126/science.1255908.
- 25. Behera, D., Chizari, S., Shaw, L.A., Porter, M., Hensleigh, R., Xu, Z., Roy, N.K., Connolly, L.G., Zheng, X. (Rayne), Saha, S., et al. (2021). Current challenges and potential directions

- towards precision microscale additive manufacturing Part II: Laser-based curing, heating, and trapping processes. Precision Engineering *68*. 10.1016/j.precisioneng.2020.12.012.
- 26. McCue, I., Benn, E., Gaskey, B., and Erlebacher, J. (2016). Dealloying and Dealloyed Materials. Annual Review of Materials Research *46*, 263–286. 10.1146/annurev-matsci-070115-031739.
- 27. Lu, X., Hasegawa, G., Kanamori, K., and Nakanishi, K. (2020). Hierarchically porous monoliths prepared via sol–gel process accompanied by spinodal decomposition. J Sol-Gel Sci Technol *95*, 530–550. 10.1007/s10971-020-05370-4.
- 28. do Rosário, J.J., Lilleodden, E.T., Waleczek, M., Kubrin, R., Petrov, A.Yu., Dyachenko, P.N., Sabisch, J.E.C., Nielsch, K., Huber, N., Eich, M., et al. (2015). Self-Assembled Ultra High Strength, Ultra Stiff Mechanical Metamaterials Based on Inverse Opals. Advanced Engineering Materials *17*, 1420–1424. 10.1002/adem.201500118.
- 29. Wang, Y., Dai, L., Ding, Z., Ji, M., Liu, J., Xing, H., Liu, X., Ke, Y., Fan, C., Wang, P., et al. (2021). DNA origami single crystals with Wulff shapes. Nature Communications 2021 12:1 *12*, 1–8. 10.1038/s41467-021-23332-4.
- 30. Rothemund, P.W.K. (2006). Folding DNA to create nanoscale shapes and patterns. Nature 2006 440:7082 440, 297–302. 10.1038/nature04586.
- 31. Rogers, W.B., Shih, W.M., and Manoharan, V.N. (2016). Using DNA to program the self-assembly of colloidal nanoparticles and microparticles. Nat Rev Mater *I*, 1–14. 10.1038/natrevmats.2016.8.
- 32. Wang, P., Meyer, T.A., Pan, V., Dutta, P.K., and Ke, Y. (2017). The Beauty and Utility of DNA Origami. Chem *2*, 359–382. 10.1016/j.chempr.2017.02.009.
- 33. Liu, W., Tagawa, M., Xin, H.L., Wang, T., Emamy, H., Li, H., Yager, K.G., Starr, F.W., Tkachenko, A.V., and Gang, O. (2016). Diamond family of nanoparticle superlattices. Science *351*, 582–586. 10.1126/science.aad2080.
- 34. Zhang, T., Hartl, C., Frank, K., Heuer-Jungemann, A., Fischer, S., Nickels, P.C., Nickel, B., and Liedl, T. (2018). 3D DNA Origami Crystals. Advanced Materials *30*, 1800273. 10.1002/adma.201800273.
- 35. Tian, Y., Zhang, Y., Wang, T., Xin, H.L., Li, H., and Gang, O. (2016). Lattice engineering through nanoparticle–DNA frameworks. Nature Mater *15*, 654–661. 10.1038/nmat4571.
- 36. Liu, X., Zhang, F., Jing, X., Pan, M., Liu, P., Li, W., Zhu, B., Li, J., Chen, H., Wang, L., et al. (2018). Complex silica composite nanomaterials templated with DNA origami. Nature 559, 593–598. 10.1038/s41586-018-0332-7.
- 37. Yan, X., Wang, Y., Ma, N., Yu, Y., Dai, L., and Tian, Y. (2023). Dynamically Reconfigurable DNA Origami Crystals Driven by a Designated Path Diagram. J. Am. Chem. Soc. *145*, 3978–3986. 10.1021/jacs.2c10755.

- 38. Dai, L., Hu, X., Ji, M., Ma, N., Xing, H., Zhu, J.-J., Min, Q., and Tian, Y. (2023). Programming the morphology of DNA origami crystals by magnesium ion strength. Proceedings of the National Academy of Sciences *120*, e2302142120. 10.1073/pnas.2302142120.
- 39. Michelson, A., Zhang, H., Xiang, S., and Gang, O. (2021). Engineered Silicon Carbide Three-Dimensional Frameworks through DNA-Prescribed Assembly. Nano Lett. *21*, 1863–1870. 10.1021/acs.nanolett.0c05023.
- 40. Michelson, A., Minevich, B., Emamy, H., Huang, X., Chu, Y.S., Yan, H., and Gang, O. (2022). Three-dimensional visualization of nanoparticle lattices and multimaterial frameworks. Science *376*, 203–207. 10.1126/science.abk0463.
- 41. Zhou, F., Sun, W., Zhang, C., Shen, J., Yin, P., and Liu, H. (2020). 3D Freestanding DNA Nanostructure Hybrid as a Low-Density High-Strength Material. ACS Nano *14*, 6582–6588. 10.1021/acsnano.0c00178.
- 42. Majewski, P.W., Michelson, A., Cordeiro, M.A.L., Tian, C., Ma, C., Kisslinger, K., Tian, Y., Liu, W., Stach, E.A., Yager, K.G., et al. (2021). Resilient three-dimensional ordered architectures assembled from nanoparticles by DNA. Science Advances 7, eabf0617. 10.1126/sciadv.abf0617.
- 43. Li, Y., Jin, H., Zhou, W., Wang, Z., Lin, Z., Mirkin, C.A., and Espinosa, H.D. (2023). Ultrastrong colloidal crystal metamaterials engineered with DNA. Science Advances 9, eadj8103. 10.1126/sciadv.adj8103.
- 44. Michelson, A., Flanagan, T.J., Lee, S.-W., and Gang, O. (2023). High-strength, lightweight nano-architected silica. Cell Reports Physical Science *4*, 101475. 10.1016/j.xcrp.2023.101475.
- 45. Douglas, S.M., Dietz, H., Liedl, T., Högberg, B., Graf, F., and Shih, W.M. (2009). Self-assembly of DNA into nanoscale three-dimensional shapes. Nature *459*, 414–418. 10.1038/nature08016.
- 46. Nguyen, L., Döblinger, M., Liedl, T., and Heuer-Jungemann, A. (2019). DNA-Origami-Templated Silica Growth by Sol–Gel Chemistry. Angewandte Chemie International Edition *58*, 912–916. 10.1002/anie.201811323.
- 47. Montemayor, L.C., and Greer, J.R. (2015). Mechanical Response of Hollow Metallic Nanolattices: Combining Structural and Material Size Effects. Journal of Applied Mechanics 82. 10.1115/1.4030361.
- 48. Zheng, X., Smith, W., Jackson, J., Moran, B., Cui, H., Chen, D., Ye, J., Fang, N., Rodriguez, N., Weisgraber, T., et al. (2016). Multiscale metallic metamaterials. Nature Materials *15*. 10.1038/nmat4694.

- 49. Guell Izard, A., Bauer, J., Crook, C., Turlo, V., and Valdevit, L. (2019). Ultrahigh Energy Absorption Multifunctional Spinodal Nanoarchitectures. Small *15*, 1903834. 10.1002/smll.201903834.
- 50. Mieszala, M., Hasegawa, M., Guillonneau, G., Bauer, J., Raghavan, R., Frantz, C., Kraft, O., Mischler, S., Michler, J., and Philippe, L. (2017). Micromechanics of Amorphous Metal/Polymer Hybrid Structures with 3D Cellular Architectures: Size Effects, Buckling Behavior, and Energy Absorption Capability. Small *13*, 1602514. 10.1002/SMLL.201602514.
- 51. Bauer, J., Hengsbach, S., Tesari, I., Schwaiger, R., and Kraft, O. (2014). High-strength cellular ceramic composites with 3D microarchitecture. Proceedings of the National Academy of Sciences of the United States of America *111*, 2453–2458. 10.1073/pnas.1315147111.
- 52. Cheng, L., Tang, T., Yang, H., Hao, F., Wu, G., Lyu, F., Bu, Y., Zhao, Y., Zhao, Y., Liu, G., et al. (2021). The Twisting of Dome-Like Metamaterial from Brittle to Ductile. Advanced Science *8*, 2002701. 10.1002/advs.202002701.
- 53. Yuan, S., Kai Chua, C., Zhou, K., Yuan, S., Chua, C.K., and Zhou, K. (2019). 3D-Printed Mechanical Metamaterials with High Energy Absorption. Advanced Materials Technologies 4, 1800419. 10.1002/ADMT.201800419.
- 54. Meza, L.R., Phlipot, G.P., Portela, C.M., Maggi, A., Montemayor, L.C., Comella, A., Kochmann, D.M., and Greer, J.R. (2017). Reexamining the mechanical property space of three-dimensional lattice architectures. Acta Materialia *140*, 424–432. 10.1016/j.actamat.2017.08.052.
- 55. Hashin, Z., and Shtrikman, S. (1963). A variational approach to the theory of the elastic behaviour of multiphase materials. Journal of the Mechanics and Physics of Solids *11*, 127–140. 10.1016/0022-5096(63)90060-7.
- 56. Tancogne-Dejean, T., Diamantopoulou, M., Gorji, M.B., Bonatti, C., and Mohr, D. (2018). 3D Plate-Lattices: An Emerging Class of Low-Density Metamaterial Exhibiting Optimal Isotropic Stiffness. Advanced Materials *30*, 1803334. 10.1002/ADMA.201803334.
- 57. Anderson, T.L. (2017). Fracture Mechanics: Fundamentals and Applications, Fourth Edition 4th ed. (CRC Press) 10.1201/9781315370293.
- 58. Bloom, K.S. (2008). Beyond the code: the mechanical properties of DNA as they relate to mitosis. Chromosoma *117*, 103–110. 10.1007/s00412-007-0138-0.
- 59. Properties: Silica Silicon Dioxide (SiO2) AZoM.com. https://www.azom.com/properties.aspx?ArticleID=1114.
- 60. Wu, J., Cheng, Q.H., Liu, B., Zhang, Y.W., Lu, W.B., and Hwang, K.C. (2012). Study on the axial compression buckling behaviors of concentric multi-walled cylindrical shells filled

- with soft materials. Journal of the Mechanics and Physics of Solids *60*, 803–826. 10.1016/j.jmps.2012.01.016.
- 61. Yan, H., Park, S.H., Finkelstein, G., Reif, J.H., and LaBean, T.H. (2003). DNA-Templated Self-Assembly of Protein Arrays and Highly Conductive Nanowires. Science *301*, 1882–1884. 10.1126/science.1089389.
- 62. Rossi, L., Sacanna, S., Irvine, W.T.M., Chaikin, P.M., Pine, D.J., and Philipse, A.P. (2011). Cubic crystals from cubic colloids. Soft Matter 7, 4139–4142. 10.1039/c0sm01246g.
- 63. Mozzi, R.L., and Warren, B.E. (1969). The structure of vitreous silica. Journal of Applied Crystallography *2*, 164–172. 10.1107/S0021889869006868.
- 64. Munetoh, S., Motooka, T., Moriguchi, K., and Shintani, A. (2007). Interatomic potential for Si–O systems using Tersoff parameterization. Computational Materials Science *39*, 334–339. 10.1016/j.commatsci.2006.06.010.
- 65. Plimpton, S. (1995). Fast Parallel Algorithms for Short-Range Molecular Dynamics. Journal of Computational Physics *117*, 1–19. 10.1006/jcph.1995.1039.
- 66. Stukowski, A. (2009). Visualization and analysis of atomistic simulation data with OVITO—the Open Visualization Tool. Modelling Simul. Mater. Sci. Eng. *18*, 015012. 10.1088/0965-0393/18/1/015012.

Figure Titles

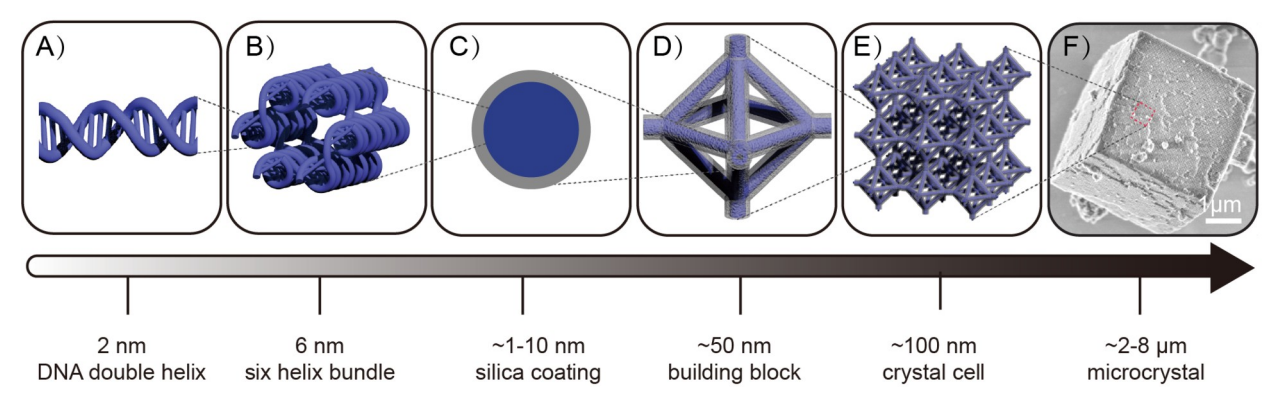


Figure 1. Multiscale DNA-silica octahedral lattice. From left to right: A.) DNA double helix strands are assembled into B.) six helix bundles. C.) A silica coating is grown onto the DNA bundle to form a core-shell structure. D.) The octahedron-based unit cell. E.) Cubic lattice structure. F.) SEM image of a DNA-silica lattice.

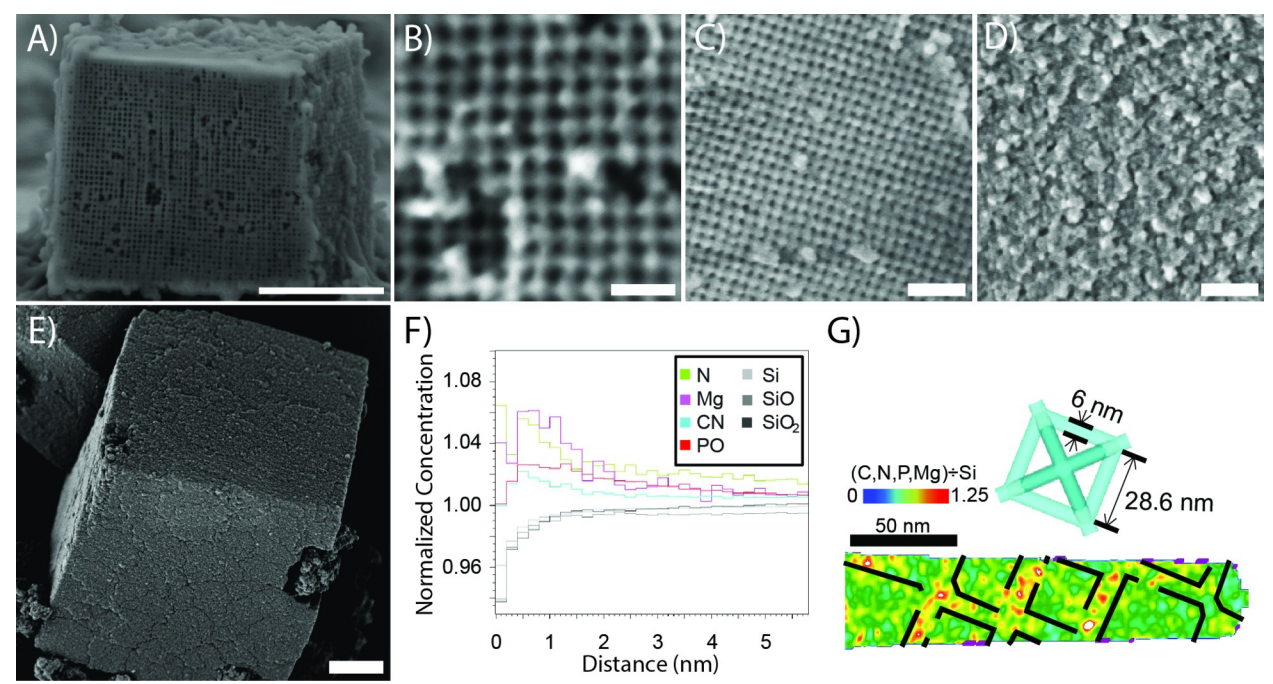


Figure 2. Structural characterization of DNA- silica lattice structures. A.) SEM image of a FIB cross sectioned lattice with 2.1 nm silica coating. B-D.) High magnification SEM images of B.) 2.1 nm, C.) 3.1 nm, and D.) space filling silica coating. E.) SEM image of lattice with space filling silica coating. F-G.) Atom probe tomography of space filling lattice. F.) Normalized radial concentration of select organic (N, Mg, CN, PO) and inorganic (Si, SiO, SiO₂) ions with respect to distance from monoatomic C ions. G.) Heatmap from a 6 nm-thick slice of the reconstructed lattice showing the ratio of organic ionic species (containing C, N, P, and/or Mg) to inorganic (species containing Si). Dashed lines indicate regions where the organic to inorganic ratio is >1. These regions resemble a cross section of the octahedral nanolattice. Scale bars: A, E.) 1 μm B.) 50 nm, C-D.) 200 nm.

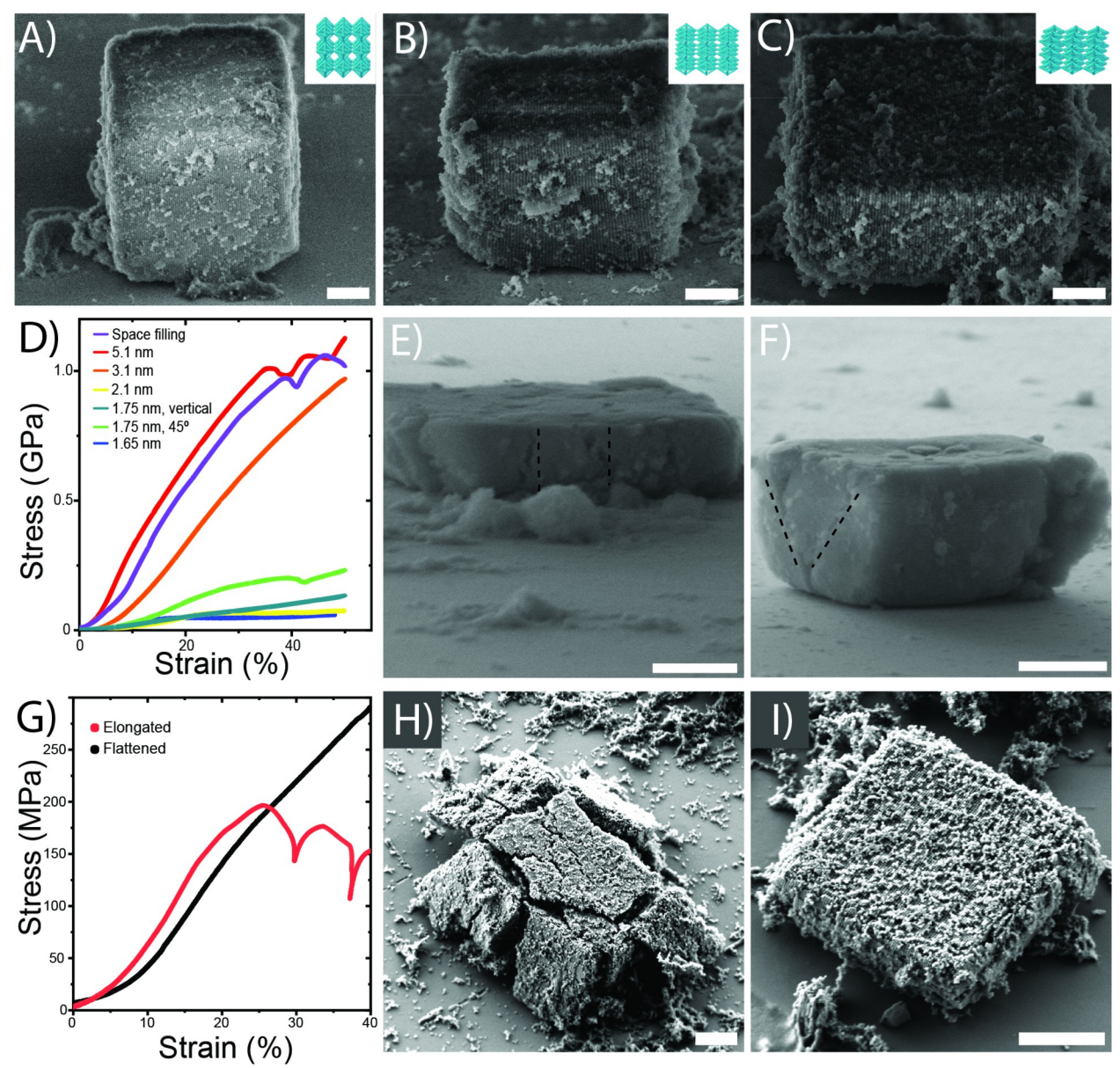


Figure 3. Compression tests of standard, elongated, and flattened lattice structures. A-C.) SEM images of A.) standard octahedron lattice, B.) elongated lattice, C.) flat lattice D.) Stress-strain curves for different silica coating thicknesses of the standard lattice. The blue curve corresponds to E.) post compression images. The vertical cracks that are formed during compression are marked with dashed lines. The green curve corresponds to F.) post compression images. The \sim 45° cracks are marked with dashed lines. G.) Stress-strain relations for the elongated and flat lattice structures. H.) post compression image for the elongated lattice. I) post compression image for the flat lattice. All scale bars are 1 μ m.

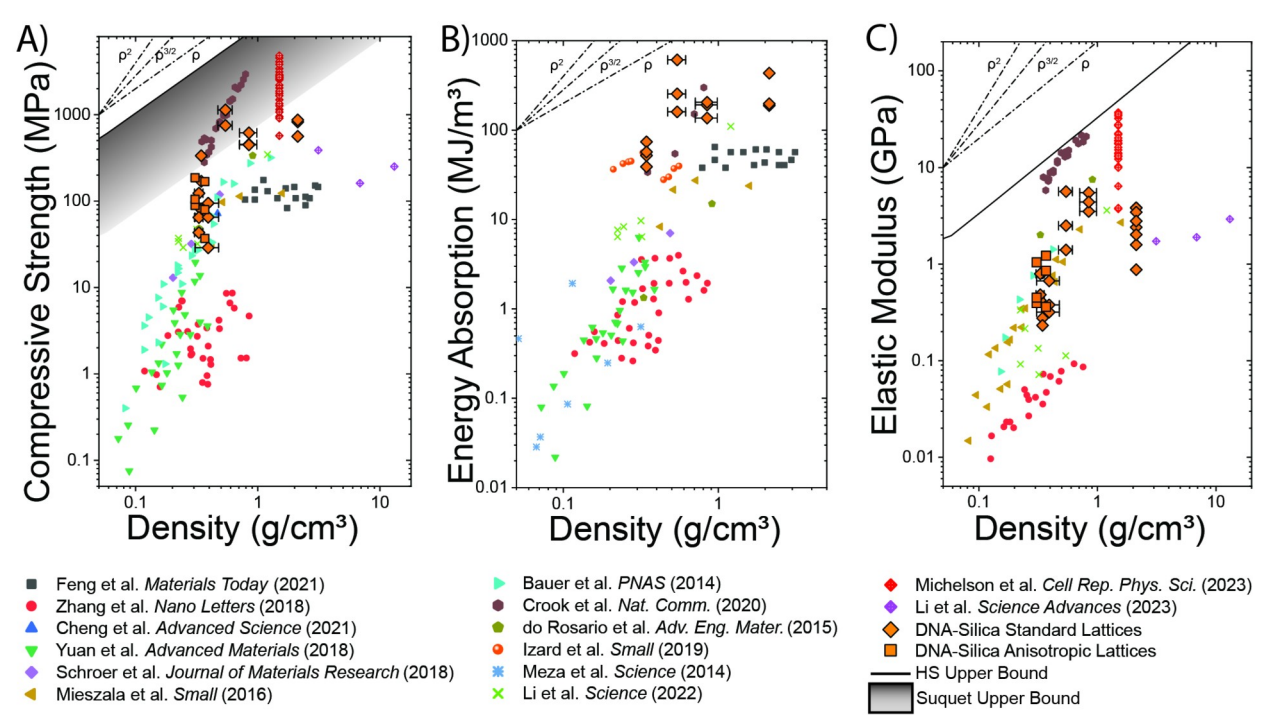


Figure 4. DNA-silica lattices compared to other nano-lattices^{1-3,8,21,24,28,43,44,49-53}. A.) Compressive strength, B.) elastic modulus, C.) energy absorption vs. density. The gradient in A shows the Suquet upper bound (equation 5). The bottom of the gradient is the Suquet prediction using the strength of bulk silica. The top of the gradient is the Suquet prediction using the theoretical maximum strength of silica. The solid black line in C is the Hashin-Shtrikman upper bound (equation 4).

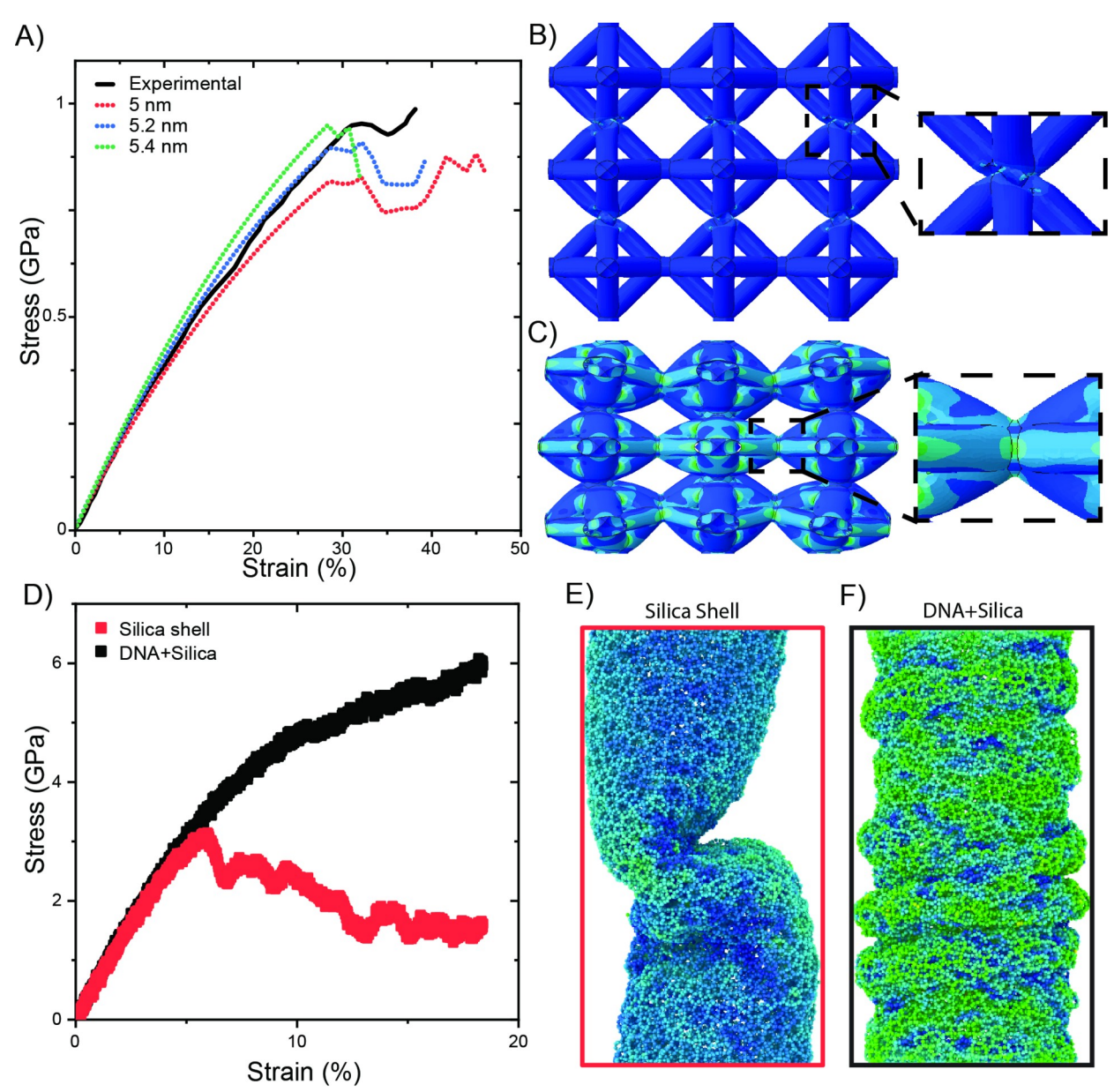


Figure 5. Computational modeling and failure mode analysis. A-C.) FEM simulation results of a 3x3x3 standard octahedral lattice made of hollow silica struts. A.) Stress-strain relations for silica shell thicknesses near 5.1 nm. B.) Lattice with 1.4 nm shell thickness fails trough vertical collapse. C.) Lattice with 4.4 nm shell thickness fails through horizontal fracture. D-F.) MD simulation results of hollow silica strut and DNA core-silica shell strut. Both struts have a 6 nm diameter and a 1 nm shell thickness. D.) Stress-strain curves for single strut in compression. E.) Kinking buckling mode for the hollow silica strut. F.) Wrinkling buckling mode for the DNA core-silica shell strut.

Video S1. Compression test for DNA-silica nanolattice with 1.75nm coating and 45° cracking.

- Video S2. Compression test for DNA-silica nanolattice with 1.75nm coating and vertical cracking.
- Video S3. Compression test for DNA-silica nanolattice with 3.1nm coating.
- Video S4. Compression test for DNA-silica nanolattice with 5.1nm coating.
- Video S5. Compression test for DNA-silica nanolattice with space filling coating.
- Table S4. Sequences of staple DNA strands for regular octahedron.
- Table S5. Sequence of sticky ends at vertexes of regular octahedron.
- Table S6. Sequences of staple DNA strands for elongated octahedron.
- Table S7. Sequence of sticky ends at vertexes of elongated octahedron.
- Table S8. Sequences of staple DNA strands for flat octahedron.
- Table S9. Sequence of sticky ends at vertexes of flat octahedron.